Resilient Free-Space Image Transmission with Helical Beams

Wei Lin,[1] Yuanhui Wen,[1] Yujie Chen ●,[1,*] Yanfeng Zhang,[1] and Siyuan Yu[1,2]

[1]*State Key Laboratory of Optoelectronic Materials and Technologies, School of Electronics and Information Technology, Sun Yat-sen University, Guangzhou, 510275, China*

[2]*Photonics Group, Merchant Venturers School of Engineering, University of Bristol, Bristol, BS8 1UB, United Kingdom*

Bendable signal transmission based on accelerating beams has become an increasingly interesting topic in recent years due to not only its fascinating propagation characteristics but also the potential to evade or resist obstructions within the transmission link. In this work, we propose a type of image-signal transmission based on nonconvex accelerating beams in contrast to convex accelerating beams such as Airy beams, which is expected to be more resilient to obstruction due to the special spectrum-position mapping characteristic. A constructed helical beam is used as the nonconvex accelerating beam for demonstration, and an image encoded in its angular spectrum is successfully retrieved after multiple self-bending without and with obstruction in the transmission link, which confirms the above idea and may open a new door for image-signal transmission in the fields of imaging, signal processing, and free-space communication.

I. INTRODUCTION

Self-accelerating beams have been widely investigated since the first experimental demonstration of Airy beams in 2007 [1,2]. Because of their intriguing properties, including nondiffracting [3–5], self-bending [6,7], and self-healing [8–11] properties, a variety of applications based on such structured light beams have been proposed, ranging from micromanipulation [12–15], micromachining [16], laser-assisted guiding of filamentation [17,18], vacuum electron acceleration [19,20], and electric discharge [21,22] to imaging [23–27] and optical communications [28]. Image signals encoded inside an Airy beam can realize self-bending transmission, which allows circumvention of obstacles during the signal transmission [25]. Furthermore, a high-speed free-space communication system based on an Airy beam has been presented, with a promising communication performance in comparison with conventional Gaussian beams in bypassing obstacles within the communication link [28].

Within the context of image-signal transmission, because of the self-healing property of accelerating beams, it would be less desired to directly encode the image signal into the real-space field distribution. Therefore, it is more suitable to encode spatial information into its angular spectrum as first proposed in Ref. [25]. However, for the convex type of accelerating beams [29–32], including Airy

beams, there is a one-to-one mapping between the spatial frequency and the position along the main lobe [33]. In this case, obstruction of the main lobe in a certain plane during transmission will greatly destroy a corresponding part of the angular spectrum, leading to the loss of the encoded image signal. To overcome this problem, the newly introduced nonconvex type of accelerating beams, such as sinusoidal or sinusoidal-based beams with multiple bendings [34–37], can be a good solution, as more than one position of the main lobe is mapped to the same spatial frequency in these beams, which are expected to be less affected if they encounter an obstruction. Therefore, it will be interesting and valuable to have a detailed investigation of image transmission based on these nonconvex accelerating beams.

In this work, we demonstrate such free-space image transmission based on our specific constructed nonconvex accelerating beam propagating along a helical trajectory. The image signal is encoded in the angular spectrum of the beam and then retrieved after multiple self-bending transmission, without or with obstruction by an obstacle of different sizes. The propagation characteristics of the helical beam and the image signal retrieved under different obstructions are thoroughly analyzed and compared with those of the Airy beam, and the findings suggest that nonconvex accelerating beams such as helical beams could enable more-resilient image-signal transmission and thus become a useful tool in future imaging and communication areas.
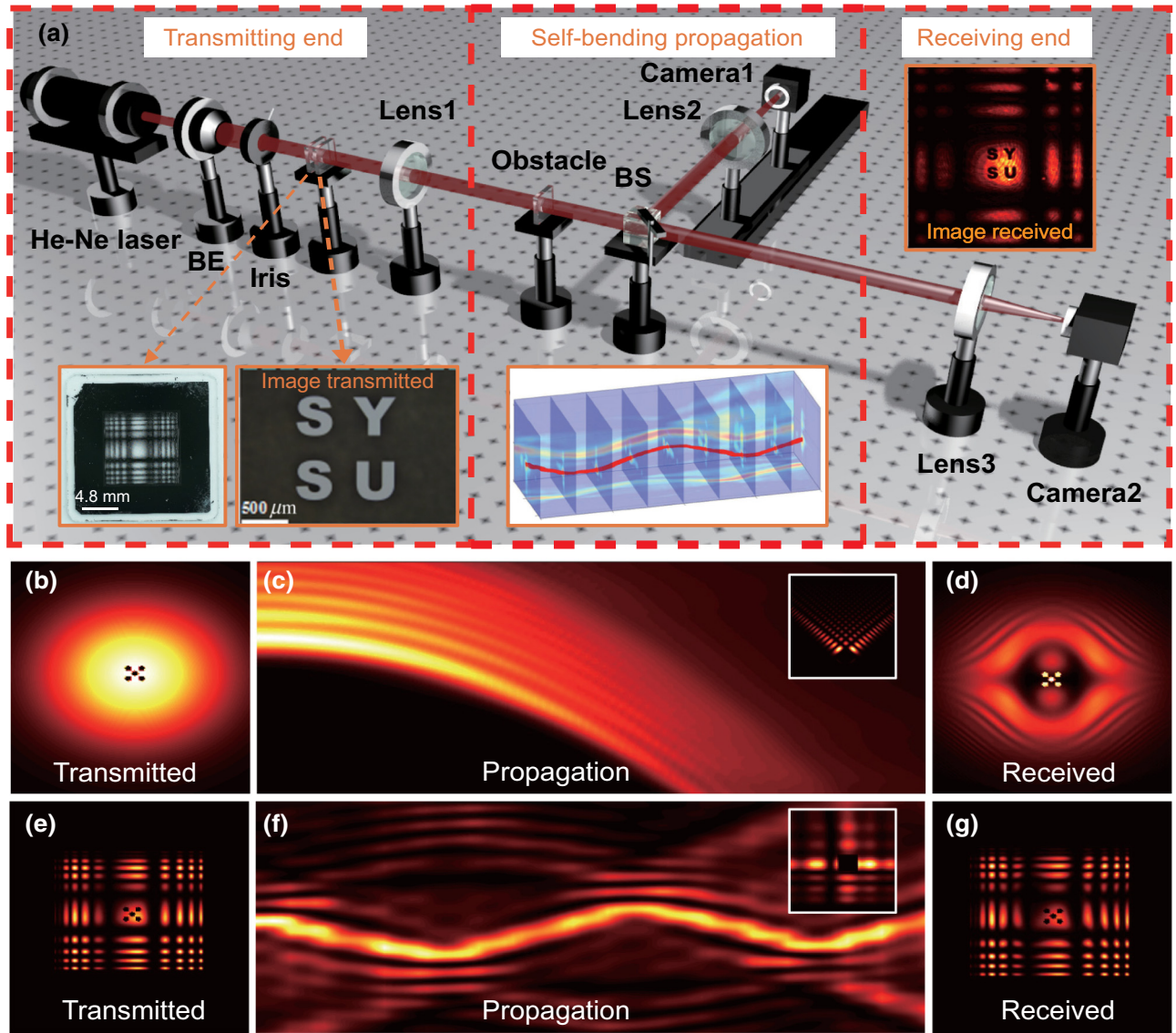
*chenyj69@mail.sysu.edu.cn

FIG. 1.   Image-signal transmission based on a nonconvex helical beam compared with the commonly used Airy beam. (a) Experimental implementation of optical image transmission based on a nonconvex accelerating beam. (b) The Fourier-space angular spectrum of the Airy beam with an encoded image. (c) Two-dimensional projection of the propagation dynamics of the Airy beam and (d) the retrieved angular spectrum of the Airy beam after blocking of its main lobe in the initial plane [as shown in the inset in (c)]. (e)–(g) Similar images as for (b)–(d) but for the case of a helical beam. BE, beam expander; BS, beam splitter.

II. THEORETICAL BACKGROUND

On the basis of plane-wave (angular-spectrum) decomposition in the paraxial regime, a light beam propagating in free space can be characterized as

$$E(x,y,z) = \int A(k_x,k_y,0) \exp\left[i\left(k_x x + k_y y - \frac{k_x^2 + k_y^2}{2k}z\right)\right] dk_x dk_y,$$

$$A(k_x,k_y,z) = A(k_x,k_y,0) \exp\left(-i\frac{k_x^2 + k_y^2}{2k}z\right),$$

(1)

where $E(x,y,z)$ is the real-space field distribution and $A(k_x,k_y,z)$ is the Fourier-space angular spectrum in plane z, k_x and k_y are spatial angular frequencies along the x and y directions, respectively, and $k = 2\pi/\lambda$ is the vacuum wave number, with $\lambda = 632.8$ nm used in this work. As can be seen in Eq. (1), during free-space propagation, the angular spectrum of the light beam simply multiplies a transfer function, which is a pure phase function corresponding to the phase shift of different plane waves. Therefore, the intensity distribution of the angular spectrum remains the same and allows handy encoding and retrieval of image signals inside. The initial angular spectrum of an accelerating beam with an image encoded can be
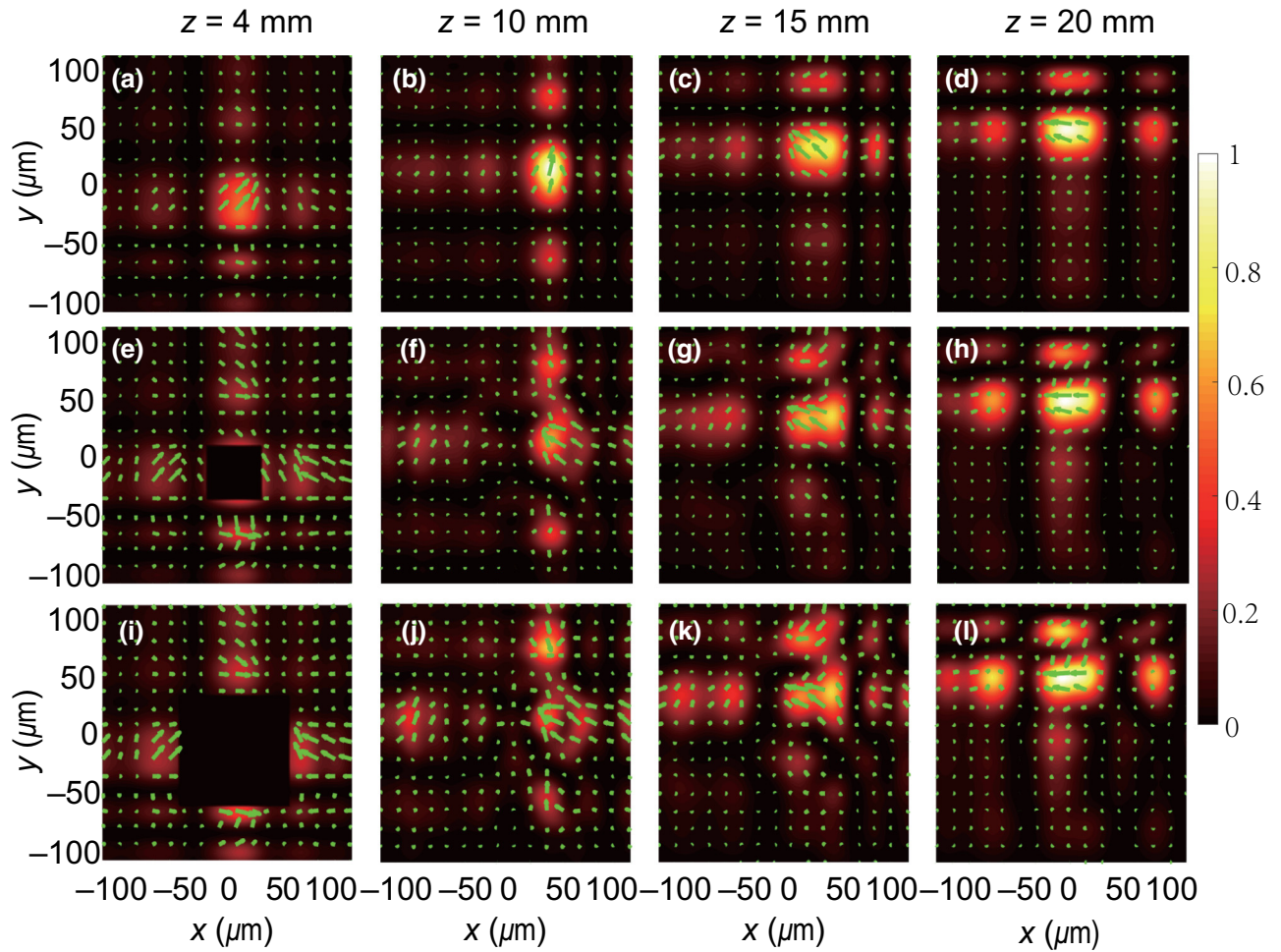
FIG. 2. Self-healing property of the helical beam under obstruction as shown by the simulated transverse energy flow of the helical beam (a)–(d) without obstruction, (e)–(h) with obstruction by an obstacle of size $50 \times 50 \, \mu m^2$ as indicated by the dark square area in (e), and (i)–(l) with obstruction by an obstacle of size $100 \times 100 \, \mu m^2$ as indicated by the dark square area in (i).

expressed as

$$A(k_x, k_y, 0) = A_0(k_x, k_y)M(k_x, k_y), \qquad (2)$$

where $M(k_x, k_y)$ represents the image and $A_0(k_x, k_y)$ is the angular spectrum of the nonconvex accelerating beam, which is designed by the superposition caustic method and is expressed as [34]:

$$A_0(k_x, k_y) = A_1(k_x)A_2(k_y)$$

$$= \left[\sum_{p=1}^{m} r_{1p}(k_x)e^{i\theta_{1p}(k_x)} \right] \left[\sum_{q=1}^{n} r_{2q}(k_y)e^{i\theta_{2q}(k_y)} \right], \qquad (3)$$

where r_{1p} and θ_{1p} are the amplitude and phase of the angular spectrum designed for the pth segment of the x-z trajectory and r_{2q} and θ_{2q} are the amplitude and phase of the angular spectrum designed for the qth segment of the y-z trajectory.

The angular spectra along both directions are separable and therefore allow respective design of the trajectory in each direction to form an eventual three-dimensional propagating trajectory. In each direction, the angular spectrum designed by the superposition caustic method is a summation of several terms responsible for different convex segments to form an integrally nonconvex trajectory. Therefore, in contrast to one-to-one spectrum-position mapping in convex accelerating beams, more than one position of the main lobe is mapped to the same spatial frequency within nonconvex accelerating beams, which are supposed to be advantageous if the main lobe is obstructed during image transmission. The obstacle located in the plane is treated as a hard-edge aperture:

$$E'(x, y, z_d) = E(x, y, z_d)O(x, y),$$

$$\text{where } O(x, y) = \begin{cases} 0, & \text{blocked area,} \\ 1, & \text{otherwise.} \end{cases} \qquad (4)$$
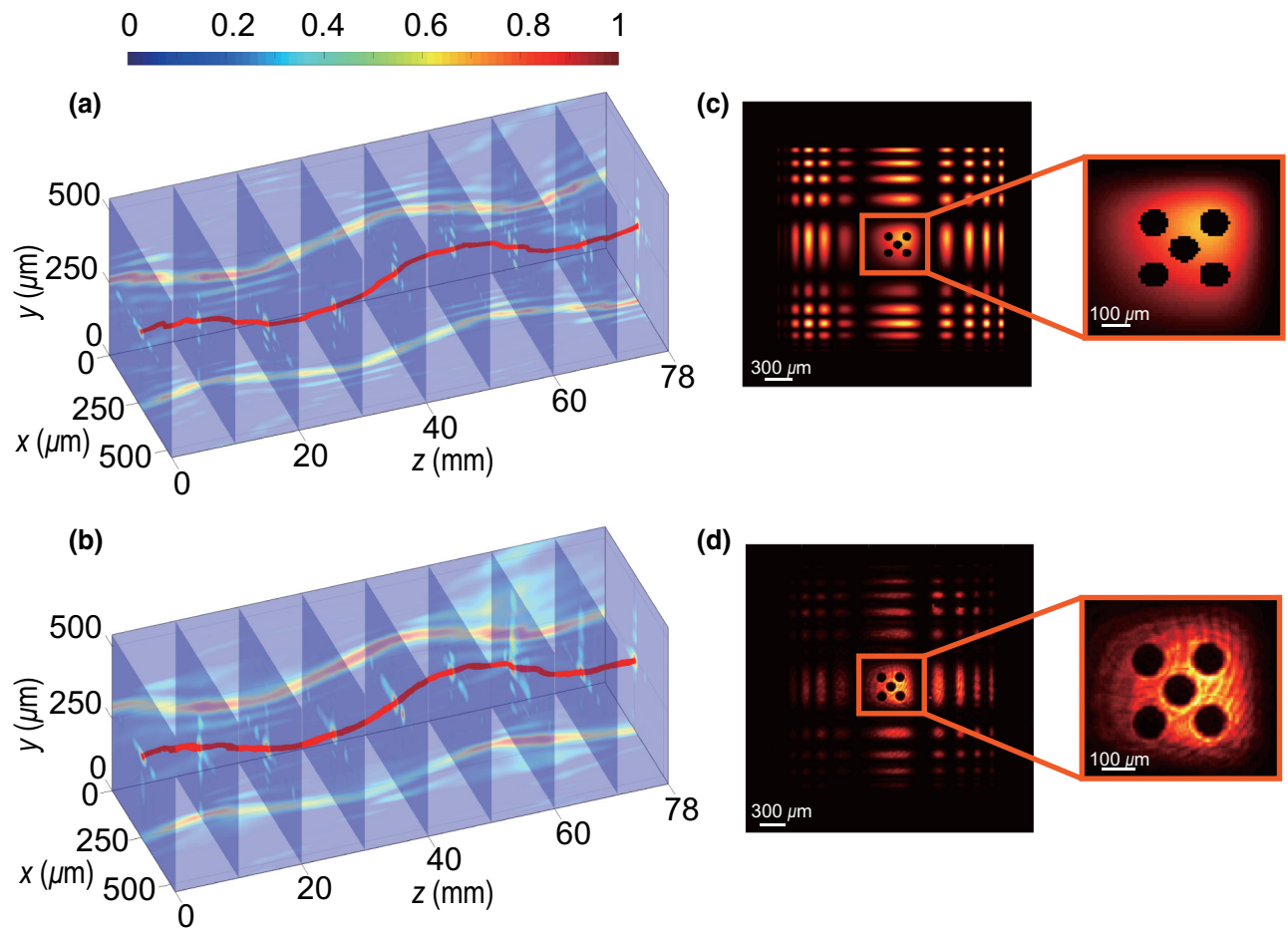
FIG. 3. Propagation of the helical beam after encoding the image signal. (a) Numerical three-dimensional propagation dynamics of the helical beam after encoding a five-dot pattern into the angular spectrum of the beam as shown in (c). (b),(d) Corresponding results from the experiment.

The field $E'(x,y,z_d)$ after obstruction continues to propagate in free space and finally is received by a detector.

The above process of image transmission is shown in Fig. 1(a). The experimental setup as illustrated is divided into three parts: transmitting end, self-bending propagation, and receiving end. At the transmitting end, a linearly polarized Gaussian beam emitted from a He-Ne laser ($\lambda = 632.8$ nm) is first enlarged and collimated by a beam expander with a magnification of $\times 10$ and then filtered out to a quasi-plane-wave by an iris. This quasi-plane-wave continues to pass through two neighboring quartz plates in succession, situated in the front focal plane of lens 1, in which the first quartz plate modulates the beam according to the angular spectrum of the designed accelerating beam (see Supplemental Material [38] Sec. I for detailed information), while the second quartz plate encodes the image signal as shown in the inset in Fig. 1(a). The beam is then Fourier transformed by lens 1 with focal length $f = 400$ mm and finally sent out. During free-space propagation, a third quartz plate with an opaque area of

chromium in different sizes acts as an obstacle to block the main lobe of the accelerating beam. The propagation dynamics of the beam is recorded by camera 1 paired with lens 2 ($f = 100$ mm) moving along a rail. Finally, at the receiving end, lens 3 ($f = 100$ mm) is used to perform the Fourier transformation and retrieve the image signal, which is recorded by camera 2 located at the back focal plane of lens 3.

Image transmissions based on convex and nonconvex accelerating beams are illustrated in Figs. 1(b)–1(g) for comparison. The same image represented by a pattern of five dots is encoded into the central angular spectra of both beams as presented in Figs. 1(b) and 1(e), respectively. Although both beams propagate along curved trajectories, the spectrum-position mapping is quite distinct. In the case of convex accelerating beams, there is one-to-one spectrum-position mapping, in which the spatial frequency is proportional to the slope of the tangent to the main lobe [39]. Therefore, if the main lobe of the beam is blocked in a certain plane during propagation, the image signal
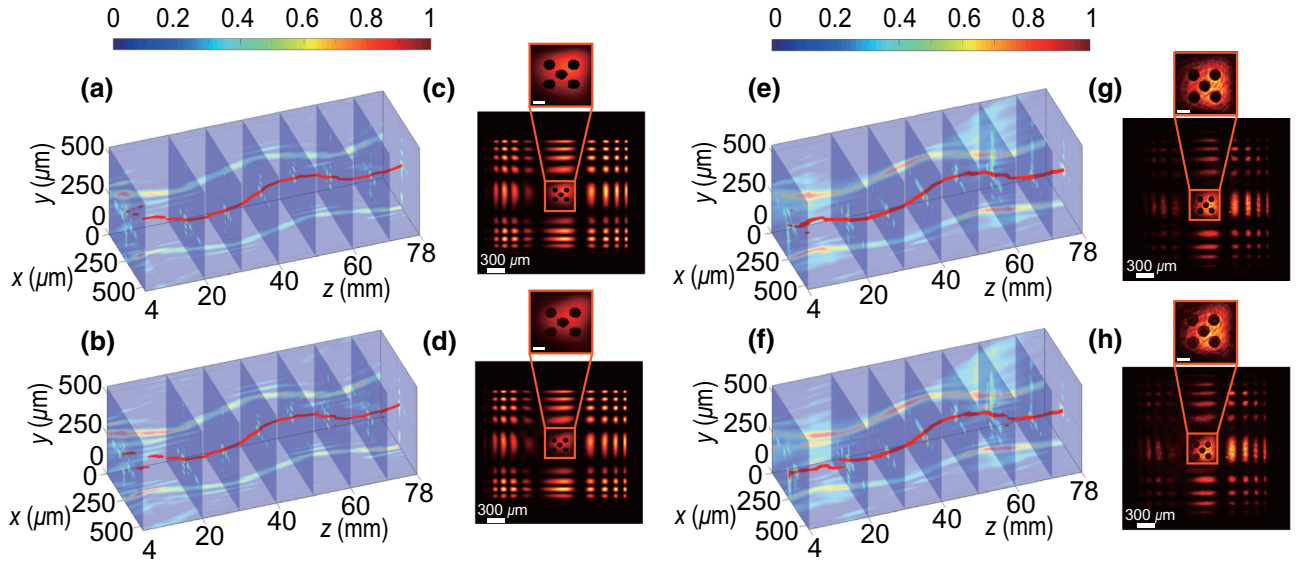
FIG. 4. Results of image transmission under obstruction. (a),(b) Numerical propagation dynamics of spectrum-encoded helical beams obstructed by obstacles of size $50 \times 50 \, \mu m^2$ and $100 \times 100 \, \mu m^2$. (c),(d) The retrieved image signals inside the spatial spectra in both cases. The corresponding results from the experiment are shown in (e)–(h). The scales in the enlarged insets are $100 \, \mu m$ for both the simulation and the experiment.

will be destroyed or even appear with contrast reversal as shown in Fig. 1(d), which occurs when the obstacle exactly acts as a high-pass filter. In contrast, in the case of nonconvex accelerating beams, multiple positions of the beam trajectory have the same slope of the tangent, which corresponds to the same spatial frequency. In this case, if the main lobe of the beam is blocked in a certain plane, the encoded image can still be retrieved clearly as shown in Fig. 1(g), and no contrast reversal appears as there are always other positions along the main lobe mapping to a low-frequency component, which demonstrates the superiority of nonconvex accelerating beams for image transmission (see Supplemental Material [38] Sec. II for a further comparison).

III. PROPAGATION CHARACTERISTICS OF HELICAL BEAMS

On the basis of the principle described above, we use a helical beam designed in our previous work [34] as the nonconvex accelerating beam for image transmission (see Supplemental Material [38] Sec. III for the propagation dynamics of the helical beam). Apart from the self-bending property, the helical beam is also self-healing under obstruction, which is revealed by the Poynting vector describing its energy-flow direction and magnitude. The time-averaged Poynting vector is expressed as [40]

$$\vec{S} = \vec{S}_\perp + \vec{S}_z = \frac{c}{8\pi}[i\omega(u\nabla_\perp u^* - u^*\nabla_\perp u) + 2\omega k|u|^2\hat{z}],$$

(5)

where $\vec{S}_\perp$ and $\vec{S}_z$ denote the transverse and longitudinal components of the Poynting vector, respectively, u is the complex-amplitude distribution of the light field, and ω is the angular frequency. On the basis of Eq. (5), Fig. 2 presents the simulated transverse components of the Poynting vector for helical beams without or with blocking by an obstacle of different sizes. As can be seen in Figs. 2(a)–2(d), the transverse energy flow of the main lobe is rotated counterclockwise, indicating a helical propagation characteristic of the beam. If the main lobe of the helical beam is blocked by an obstacle, it is shown in Figs. 2(e) and 2(i) that considerable energy residing in the side lobes near the original main lobe will flow in. After a certain propagation distance, the main lobe finally recovers, as shown in Figs. 2(d), 2(h), and 2(l), and this propagation distance required for self-healing also increases with the size of the obstacle.

IV. IMAGE TRANSMISSION WITH HELICAL BEAMS

For demonstration of image transmission, a pattern of five dots is encoded into the angular spectrum of the helical beam at the transmitting end as illustrated in Fig. 1. The propagation dynamics of this spectrum-encoded helical beam recoded by camera 1 is presented in Fig. 3(b), including the propagation trajectory, cross section and projected intensity distributions. It is interesting to note that although the low-frequency components of the angular spectrum are modulated to encode the image, the propagation characteristics of this spectrum-encoded helical beam
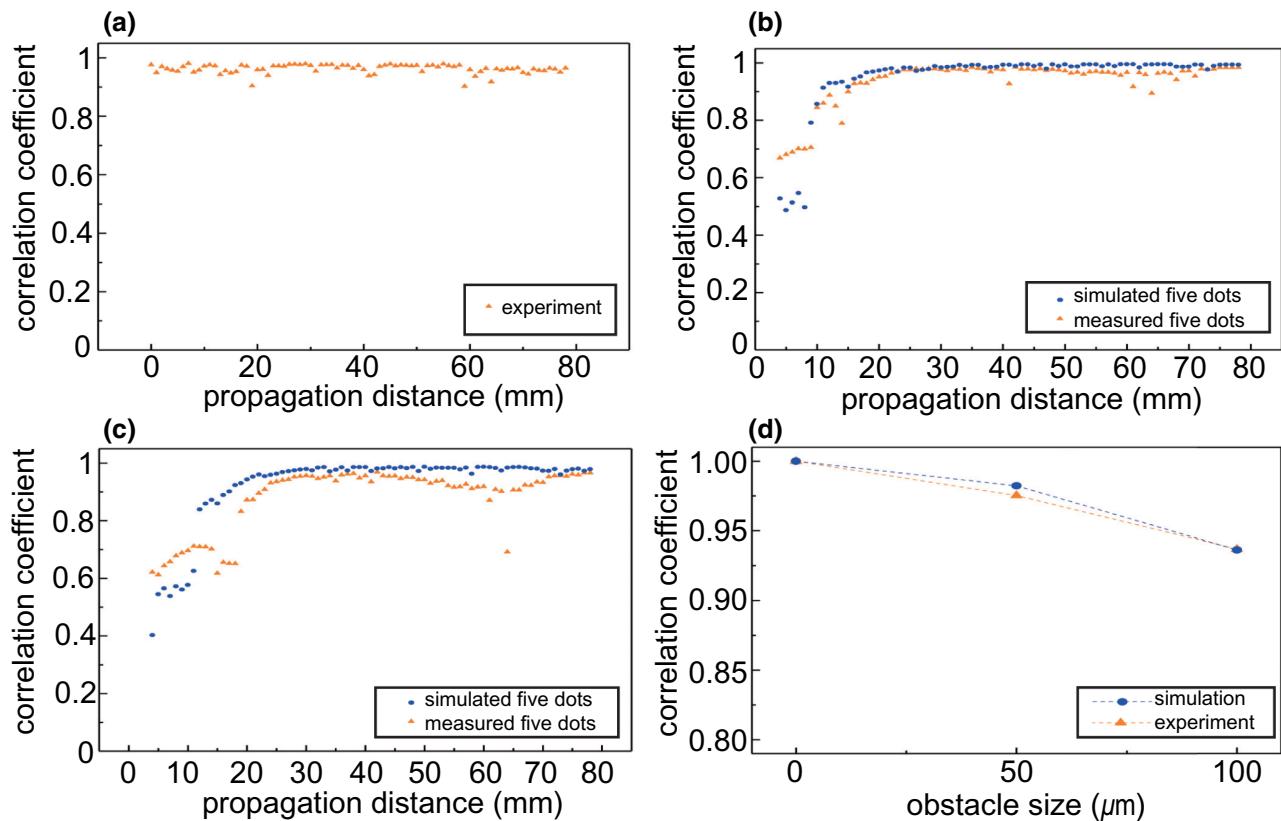
FIG. 5. (a) Correlation coefficient between helical beams before and after image encoding in the angular spectrum in different propagation planes. (b),(c) Correlation coefficient between spectrum-encoded helical beams without and with obstruction by an obstacle of size (b) $50 \times 50 \, \mu\text{m}^2$ and (c) $100 \times 100 \, \mu\text{m}^2$. (d) Correlation coefficient between the retrieved image and the original image without and with obstruction by an obstacle of different sizes.

are almost the same as those without modulation, which confirms the feasibility of image encoding in the angular spectrum of the light beam. Furthermore, the image is retrieved and recorded by camera 2 [see Fig. 3(d)]. As can be seen, the image is retrieved clearly after self-bending propagation, and the experimental result matches well with the corresponding numerical result as illustrated in Figs. 3(a) and 3(c), which successfully demonstrate image-signal transmission based on a nonconvex helical beam.

V. IMAGE TRANSMISSION UNDER OBSTRUCTION

After the above demonstration, it would be interesting and is necessary to further find out the influence of an obstacle in the image-signal-transmission process described above. Two obstacles with sizes of $50 \times 50 \, \mu\text{m}^2$ (the size of the main lobe) and $100 \times 100 \, \mu\text{m}^2$ (see Supplemental Material [38] Sec. IV for the results for obstacles with other sizes) are used to block the main lobe of the helical beam in the $z = 4$ mm plane (see Supplemental Material [38] Sec. IV for the results for obstruction located at different positions). The helical trajectory of the main

lobe breaks up after obstruction known as the "caustic hole" [41], while after a certain propagation distance, it appears again due to the self-healing property and the distance for recovery increases with the size of the obstacle as mentioned before. More importantly, although the main lobe of the helical beam is obstructed during propagation, the image encoded in the angular spectrum can still be retrieved and the influence of the obstacle on the image seems to be simply the energy loss related to the size of the obstacle. The experimental results agree well with the numerical ones in Fig. 4.

For a quantitative analysis, a two-dimensional correlation function is introduced to quantify the similarities among the original helical beam, the spectrum-encoded helical beam, the obstructed helical beam, and the images encoded in these beams, and is defined as

$$C = \frac{\iint [I_1(x,y) - \bar{I}_1][I_2(x,y) - \bar{I}_2] dx dy}{\sqrt{\iint [I_1(x,y) - \bar{I}_1]^2 dx dy \iint [I_2(x,y) - \bar{I}_2]^2 dx dy}},$$
(6)

where $I_1(x,y)$ and $I_2(x,y)$ are two intensity distributions of the light beam in real space or the Fourier domain, with

$\bar{I}_1$ and $\bar{I}_2$ being average intensity values. The correlation coefficient between the original helical beam and the spectrum-encoded helical beam is shown in Fig. 5(a). The correlation coefficients are all greater than 0.9 and are mostly greater than 0.95 in different propagation planes, which means the image encoded in the angular spectrum has little influence on the propagation dynamics of the helical beam and thus justifies such an image-encoding scheme. Furthermore, the correlation coefficients between the spectrum-encoded helical beam and the obstructed helical beams are presented in Figs. 5(b) and 5(c). The process after obstruction can be roughly divided into three stages. In the first stage, within the caustic hole, the correlation coefficient is very low and varies randomly. In the second stage, after getting out of the caustic hole, there is a transition region where the main lobe gradually recovers and thus the correlation coefficient increases constantly. In the last stage, the correlation coefficient returns to a high value and becomes relatively stable. The first two stages get longer as the size of the obstacle increases, which is consistent with the previous discussion. Finally, the most-important correlation coefficient, between the retrieved images without and with obstruction, is shown in Fig. 5(d), which quantitatively describes the influence of the obstacle on the encoded image. It is found that as the obstacle gets larger, the correlation coefficient of the retrieved images decreases slightly but the value still remains high, which confirms the resistance to obstruction for image-signal transmission based on a nonconvex accelerating beam.

VI. CONCLUSION

In summary, image-signal transmission based on nonconvex accelerating beams is proposed and demonstrated. It is theoretically proposed that image-signal transmission based on nonconvex accelerating beams is more resilient to obstruction due to their special spectrum-position mapping in contrast to the one-to-one mapping in convex accelerating beams such as Airy beams. To confirm this idea, a previously constructed helical beam is used as the nonconvex accelerating beam and its propagation dynamics, especially the self-healing property, are described. On the basis of this helical beam, the image of a five-dot pattern as an example is encoded into the angular spectrum of the beam and then retrieved after multiple self-bending processes, successfully demonstrating image-signal transmission based on a nonconvex accelerating beam. Furthermore, it is found that image-signal transmission based on the helical beam indeed resists obstruction during propagation as expected, which confirms its reliability, and it might be especially useful in future imaging and communication areas, such as astronomical signal transmission and microscopic image transmission.

[1] G. A. Siviloglou, J. Broky, A. Dogariu, and D. N. Christodoulides, Observation of Accelerating Airy Beams, Phys. Rev. Lett. **99**, 213901 (2007).

[2] G. A. Siviloglou and D. N. Christodoulides, Accelerating finite energy airy beams, Opt. Lett. **32**, 979 (2007).

[3] I. M. Besieris and A. M. Shaarawi, A note on an accelerating finite energy airy beam, Opt. Lett. **32**, 2447 (2007).

[4] J. C. Gutiérrez-Vega, M. D. Iturbe-Castillo, and S. Chávez-Cerda, Alternative formulation for invariant optical fields: Mathieu beams, Opt. Lett. **25**, 1493 (2000).

[5] M. A. Bandres, J. C. Gutiérrez-Vega, and S. Chávez-Cerda, Parabolic nondiffracting optical wave fields, Opt. Lett. **29**, 44 (2004).

[6] G. A. Siviloglou, J. Broky, A. Dogariu, and D. N. Christodoulides, Ballistic dynamics of airy beams, Opt. Lett. **33**, 207 (2008).

[7] Y. Hu, P. Zhang, C. Lou, S. Huang, J. Xu, and Z. Chen, Optimal control of the ballistic motion of airy beams, Opt. Lett. **35**, 2260 (2010).

[8] J. Broky, G. A. Siviloglou, A. Dogariu, and D. N. Christodoulides, Self-healing properties of optical airy beams, Opt. Express **16**, 12880 (2008).

[9] X. Chu, G. Zhou, and R. Chen, Analytical study of the self-healing property of airy beams, Phys. Rev. A **85**, 013815 (2012).

[10] L. Zhang, F. Ye, M. Cao, D. Wei, P. Zhang, H. Gao, and F. Li, Investigating the self-healing property of an optical airy beam, Opt. Lett. **40**, 5066 (2015).

[11] F. Zhuang, Z. Zhu, J. Margiewicz, and Z. Shi, Quantitative study on propagation and healing of airy beams under experimental conditions, Opt. Lett. **40**, 780 (2015).

[12] P. Zhang, J. Prakash, Z. Zhang, M. S. Mills, N. K. Efremidis, D. N. Christodoulides, and Z. Chen, Trapping and guiding microparticles with morphing autofocusing airy beams, Opt. Lett. **36**, 2883 (2011).

[13] P. Zhang, Z. Zhang, J. Prakash, S. Huang, D. Hernandez, M. Salazar, D. N. Christodoulides, and Z. Chen, Trapping and transporting aerosols with a single optical bottle beam generated by moiré techniques, Opt. Lett. **36**, 1491 (2011b).

[14] J. Baumgartl, M. Mazilu, and K. Dholakia, Optically mediated particle clearing using airy wavepackets, Nat. Photonics **2**, 675 (2008).

[15] J. Zhao, I. D. Chremmos, D. Song, D. N. Christodoulides, N. K. Efremidis, and Z. Chen, Curved singular beams for three-dimensional particle manipulation, Sci. Rep. **5,** 12086 (2015).

[16] A. Mathis, F. Courvoisier, L. Froehly, L. Furfaro, M. Jacquot, P. A. Lacourt, and J. M. Dudley, Micromachining along a curve: Femtosecond laser micromachining of curved profiles in diamond and silicon using accelerating beams, Appl. Phys. Lett. **101,** 071110 (2012).

[17] P. Polynkin, M. Kolesik, and J. Moloney, Filamentation of Femtosecond Laser airy Beams in Water, Phys. Rev. Lett. **103,** 123902 (2009).

[18] P. Polynkin, M. Kolesik, J. V. Moloney, G. A. Siviloglou, and D. N. Christodoulides, Curved plasma channel generation using ultraintense airy beams, Science **324,** 229 (2009).

[19] J. Li, W. Zang, and J. Tian, Vacuum laser-driven acceleration by airy beams, Opt. Express **18,** 7300 (2010).

[20] J. Li, W. Zang, and J. Tian, Analysis of electron capture acceleration channel in an airy beam, Opt. Lett. **35,** 3258 (2010).

[21] M. Clerici, Y. Hu, P. Lassonde, C. Milián, A. Couairon, D. N. Christodoulides, Z. Chen, L. Razzari, F. Vidal, F. Légaré, D. Faccio, and R. Morandotti, Laser-assisted guiding of electric discharges around objects, Sci. Adv. **1,** e1400111 (2015).

[22] N. Horiuchi, Laser-guided sparks, Nat. Photonics **9,** 488 (2015).

[23] S. Jia, J. C. Vaughan, and X. Zhuang, Isotropic three-dimensional super-resolution imaging with a self-bending point spread function, Nat. Photonics **8,** 302 (2014).

[24] T. Vettenburg, H. I. C. Dalgarno, J. Nylk, C. Coll-Lladó, D. E. K. Ferrier, T. Cizmár, F. J. Gunn-Moore, and K. Dholakia, Light-sheet microscopy using an airy beam, Nat. Methods **11,** 541 (2014).

[25] Y. Liang, Y. Hu, D. Song, C. Lou, X. Zhang, Z. Chen, and J. Xu, Image signal transmission with airy beams, Opt. Lett. **40,** 5686 (2015).

[26] B. Schroeder and S. Jia, Frequency analysis of a self-bending point spread function for 3D localization-based optical microscopy, Opt. Lett. **40,** 3189 (2015).

[27] Z. Cai, Y. Liu, Y. Hu, C. Zhang, J. Xu, S. Ji, J. Ni, Z. Lao, J. Li, Y. Zhao, D. Wu, and J. Chu, Generation of colorful airy beams and airy imaging of letters via two-photon processed cubic phase plates, Opt. Lett. **43,** 1151 (2018).

[28] G. Zhu, Y. Wen, X. Wu, Y. Chen, J. Liu, and S. Yu, Obstacle evasion in free-space optical communications utilizing airy beams, Opt. Lett. **43,** 1203 (2018).

[29] E. Greenfield, M. Segev, W. Walasik, and O. Raz, Accelerating Light Beams along Arbitrary Convex Trajectories, Phys. Rev. Lett. **106,** 213902 (2011).

[30] L. Froehly, F. Courvoisier, A. Mathis, M. Jacquot, L. Furfaro, R. Giust, P. A. Lacourt, and J. M. Dudley, Arbitrary accelerating micron-scale caustic beams in two and three dimensions, Opt. Express **19,** 16455 (2011).

[31] Y. Hu, D. Bongiovanni, Z. Chen, and R. Morandotti, Multipath multicomponent self-accelerating beams through spectrum-engineered position mapping, Phys. Rev. A **88,** 043809 (2013).

[32] D. Bongiovanni, Y. Hu, B. Wetzel, R. A. Robles, G. Mendoza González, E. A. Marti-Panameño, Z. Chen, and R. Morandotti, Efficient optical energy harvesting in self-accelerating beams, Sci. Rep. **5,** 13197 (2015).

[33] Y. Hu, D. Bongiovanni, Z. Chen, and R. Morandotti, Multipath multicomponent self-accelerating beams through spectrum-engineered position mapping, Phys. Rev. A **88,** 043809 (2013).

[34] Y. Wen, Y. Chen, Y. Zhang, H. Chen, and S. Yu, Winding light beams along elliptical helical trajectories, Phys. Rev. A **94,** 013829 (2016).

[35] Y. Wen, Y. Chen, Y. Zhang, H. Chen, and S. Yu, Tailoring accelerating beams in phase space, Phys. Rev. A **95,** 023825 (2017).

[36] Y. Wen, Y. Chen, Y. Zhang, and S. Yu, Highly adjustable helical beam: Design and propagation characteristics (invited paper), Chin. Opt. Lett. **15,** 030011 (2017).

[37] Y. Wen, Y. Chen, and S. Yu, Design of accelerating beams based on caustic method, Acta Phys. Sin. **66,** 144210 (2017).

[38] See Supplemental Material at http://link.aps.org/supplemental/10.1103/PhysRevApplied.12.044058 for further simulation and experimental results.

[39] P. Vaveliuk, A. Lencina, J. A. Rodrigo, and O. M. Matos, Caustics, catastrophes, and symmetries in curved beams, Phys. Rev. A **92,** 033850 (2015).

[40] L. Allen, M. Padgett, and M. Babiker, in *Progress in Optics* (Elsevier, North-Holland, 1999), p. 291.

[41] P. Vaveliuk, Ó. Martńez-Matos, Y. Ren, and R. Lu, Dual behavior of caustic optical beams facing obstacles, Phys. Rev. A **95,** 063838 (2017).